

A geometrical comparison of the momentum-carrying structures between boundary layer transition and fully developed turbulence

By A. Elnahas, A. Lozano-Durán[†] AND J. Wallace[‡]

The late stages of boundary layer transition are characterized by the rapid breakdown of organized, coherent structures such as Λ -vortices into fully broadband turbulence. This breakdown can take effect at a repeatable, localized region in space, as is the case with the natural H-type and K-type transition simulated by Sayadi *et al.* (2013), or sporadically in space, forming turbulent spots, due to freestream turbulence forcing, as was simulated by Wu *et al.* (2017). In both cases, the conditional single-point turbulent statistics within the late breakdown stages resemble those of fully developed turbulence, suggesting that they could be simpler building blocks of fully developed wall-bounded turbulent flows. This report aims to extend this comparison beyond single-point statistics to the geometrical aspects of the dominant momentum-carrying structures. Utilizing a direct numerical simulation of an H-type transition, the structure identification algorithm of Lozano-Durán *et al.* (2012) is used to isolate contiguous regions in space belonging to each of the four Reynolds shear stress quadrants (Wallace *et al.* 1972). The geometrical properties of the identified structures, such as their aspect ratios, occupied volume as a function of their height, and fractal dimensions, as well as their surrounding conditional flow fields, are examined as a function of the eddy-turnover length downstream of the breakdown of the Λ -vortices into broadband turbulence. It is found that all the examined geometrical scaling laws of dominant momentum-carrying structures, namely ejections and sweeps, recover those from fully developed turbulent channel flow within less than one-third of an eddy-turnover length. The conditional flow fields highlight that the main difference downstream of the transition point is the spatial organization of the ejections and sweeps, changing from symmetric pairs to single-sided pairs as the flow gets more turbulent.

1. Introduction

In the late stages of boundary layer transition, localized packets of turbulence emerge, grow, and coalesce to form the front of the turbulent boundary layer. These localized packets, or turbulent spots, have long been supposed to be more ordered versions of the structures found in developed wall-bounded turbulence. Research into turbulent spots spans over seven decades since being observed and called spots by Emmons (1951). Kinematic studies of the structure and conditional statistics within and around turbulent spots have been extensive, ranging from the works of Cantwell *et al.* (1978) and Henningson *et al.* (1987) to the more recent studies of Park *et al.* (2012) and Marxen & Zaki (2019). One of the conclusions from these studies is that conditioned on being within the spot,

[†] Department of Aeronautics & Astronautics, Massachusetts Institute of Technology

[‡] Department of Mechanical Engineering & Institute for Physical Science and Technology, University of Maryland, College Park

the primary single-point statistics of wall-bounded turbulent shear flows are recovered, namely the mean velocity profile, turbulence intensity and enstrophy distributions, and turbulent kinetic energy budgets. The similarity of these fundamental turbulence statistics, coupled with the visual observation that spots are isolated and appear ordered, led the community to hypothesize that reduced-order models of near-wall turbulence based on the kinematics and dynamics of turbulent spots are theoretically achievable. Observations of the similarities between transitional–turbulent and turbulent–turbulent spots that emerge and lie deep within the turbulent boundary layer by Wu *et al.* (2017) provide evidence for the dynamical link. Such conditional statistics have also been compared within the ordered regions of naturally transitioning boundary layers through H-type and K-type transition with similar observations by Sayadi *et al.* (2013). A comprehensive review of the current understanding of turbulent spots is presented by Wu (2022).

Understanding the kinematics and dynamics of the turbulent structures responsible for transporting momentum within wall-bounded turbulent shear flows is essential for theoretical model development. The primary coherent structures that transport momentum across the turbulent wall layer, namely ejections and sweeps, have been observed in the seminal studies of Kline *et al.* (1967) and Corino & Brodkey (1969). The aggregate statistical characteristics of all these ejections and sweeps within a flow can be obtained by decomposing the streamwise and wall-normal velocity fluctuations into quadrants based on their sign combinations as was first done by Wallace *et al.* (1972). By extending the standard quadrant analysis technique to three-dimensional connected regions in space, Lozano-Durán *et al.* (2012) was able to extract structural information about the momentum-carrying structures in fully developed turbulent channel flows, elucidating their spatial organization, characteristic scales, and geometric shapes. While the single-point statistics extracted from turbulent spots and late-stage natural transition resemble those of fully developed turbulence, it is yet to be established if the structural statistics of the momentum-carrying eddies within these regions follow the same geometrical scaling laws as that of fully developed turbulence. The purpose of this study is to establish that comparison quantitatively.

The report is organized as follows. Section 2 describes the direct numerical simulation (DNS) transitioning boundary layer data used for the analysis, a summary of the algorithm used to extract the momentum-carrying structures, and some aggregate information about these structures. Section 3 characterizes the geometrical statistics of the identified structures as a function of the downstream distance from the point of breakdown of the Λ -vortices. The conditional flow fields surrounding the identified structures are examined in Section 4. Finally, conclusions are presented in Section 5.

2. DNS dataset and the structure identification algorithm

2.1. H-type naturally transitioning boundary layer

Motivated by the similarities to developed turbulence in the one-point statistical quantities, such as the mean velocity profiles and Reynolds shear stresses in the H-type transition scenario of Sayadi *et al.* (2013), a similar set-up is used here to extract and analyze the momentum-carrying eddies. In this flow, x , y , and z correspond to the streamwise, wall-normal, and spanwise directions, respectively, with U and u , V and v , and W and w being the corresponding total and fluctuating velocities in each direction. The DNS is simulated using the set-up of Lozano-Durán *et al.* (2018), with the exception that the

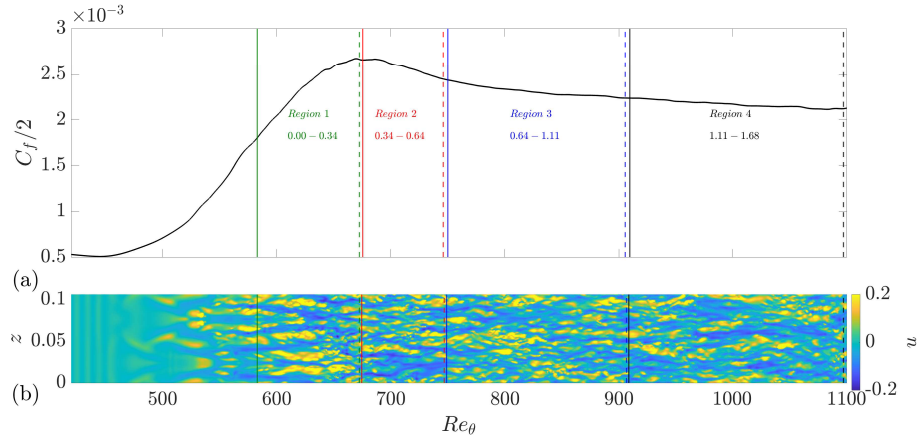


FIGURE 1. (a) The skin-friction coefficient as a function of the momentum thickness-based Reynolds number, Re_θ . The domain is partitioned into four regions with the associated eddy-turnover distance, \tilde{x} , from the chosen location labeled. The color coding used to identify the region is consistent throughout the rest of the report. (b) The near-wall streamwise velocity streaks at a wall-normal distance corresponding to $y^+ \equiv yu_\tau/\nu|_{Re_\theta=900} = 5$.

spanwise extent is equal to a single oblique disturbance wavelength as is the case for flow analyzed by Elnahhas *et al.* (2019) and Elnahhas & Johnson (2022).

Figure 1 shows the skin-friction coefficient of the transitional boundary layer DNS used to extract the structures, along with an instantaneous snapshot of the near-wall streamwise velocity streaks. The domain is partitioned into four regions with the associated dimensionless eddy-turnover distance, \tilde{x} , defined as

$$\tilde{x} = \int^x [dx/(\delta U_\infty^+)] \quad (2.1)$$

per Sillero *et al.* (2013), labelled on the plot. The origin of this distance is chosen to be the location where the Λ -vortices first break down. Region one starts at this breakdown location and ends at the skin-friction peak. Region two starts at the skin-friction peak location and ends at $Re_\theta = 750$, which is the location where the turbulent intensities first match fully developed turbulence up to 200 inner units, which is not shown for brevity. Region three extends from $Re_\theta = 750$ to $Re_\theta \approx 900$, where Sayadi *et al.* (2013) had established that the mean one-point statistics are independent of the transition scenario. Region four covers the rest of the domain.

2.2. Momentum-carrying structure identification algorithm

The clustering algorithm developed by Lozano-Durán *et al.* (2012) is adapted for a two-dimensional spatially varying mean flow field. At each point in space and time, the absolute value of the instantaneous fluctuating turbulent stress, $\tau = uv$, is compared to the local mean turbulence intensity product scaled with a factor, H , known as the hyperbolic hole size

$$|\tau| > H u'(x, y) v'(x, y), \quad (2.2)$$

where $u'(x, y)$ and $v'(x, y)$ are the two-dimensionally varying turbulence intensity fields in this boundary layer flow. A minimal threshold is also applied due to the turbulent/non-turbulent boundary layer interface with the freestream flow. This study uses a value of

$H = 1.75$ after conducting a percolation analysis, as was done by Lozano-Durán *et al.* (2012).

For all points that satisfy the criteria, the clustering algorithm connects those that are neighbors on the computational grid. For each of these clusters, the average streamwise, u_m , and wall-normal, v_m , velocities can be computed over the occupied volume of the cluster, Ω , as

$$u_m = \frac{\int_{\Omega} u dV}{\int_{\Omega} dV} \quad \text{and} \quad v_m = \frac{\int_{\Omega} v dV}{\int_{\Omega} dV}, \quad (2.3)$$

which allows each cluster to be associated with a particular Reynolds stress quadrant, with Q2 events (ejections) corresponding to $u_m < 0$ and $v_m > 0$ and Q4 events (sweeps) corresponding to $u_m > 0$ and $v_m < 0$. The other two quadrants, namely Q1 and Q3, correspond to counter-gradient shear stress events and are less important for momentum transfer. Hence, the quadrant analysis of Wallace *et al.* (1972) is extended to three-dimensional objects within the flow field. The hyperbolic criterion guarantees that all connected points of a single cluster belong to the same quadrant. For each of these clusters, information such as their size in each direction, whether they are attached to the wall, occupied volume, fractal dimension, and the surrounding flow field are extracted and analyzed in the following sections.

2.3. The number and volume fractions of the identified structures

The structure identification algorithm was applied to 130 instantaneous flow fields, which span approximately 16 eddy-turnover times at the location corresponding to $Re_{\theta} = 900$, where Sayadi *et al.* (2013) had established that this transition scenario fully recovers the one-point turbulent statistics of the fully developed flow. Within each of the regions identified in Figure 1, the number fraction of the identified structures and the volume fraction occupied by the structures with respect to the volume of the mean turbulent boundary layer within that region are reported in Table 1.

The volume fractions of the attached clusters, defined as those whose wall-normal extent begins below $y^+ = 20$ defined in the local plus units of their centroids, resemble those of the fully developed channel flows analyzed by Lozano-Durán *et al.* (2012) in all regions. This is unexpected given that the downstream end of the first region is less than one-third of an eddy-turnover length after the breakdown of the organized Λ -vortices. The primary difference between the values extracted from the current flow and those extracted from the fully developed turbulent channel flow is the elevated number fraction of Q4 (sweep) events across the entire streamwise extent of the boundary layer, whether attached or not.

3. Geometrical analysis of the dominant momentum-carrying structures

This section discusses the basic geometric properties of the dominant momentum-carrying structures as a function of the downstream distance from the point of breakdown. Based on the substantial similarity between the number and volume fractions of attached eddies presented in Table 1 and their counterparts for fully developed turbulent channel flow, we focus on the geometric properties of those structures, as they are the largest and transport the most momentum. Almost all attached structures are either sweeps (Q4) or ejections (Q2). Thus, only statistics concerning these two types of motions are presented.

Region	N_1	N_2	N_3	N_4	V_1	V_2	V_3	V_4
1 (all)	0.10	0.31	0.07	0.52	0.003	0.085	0.008	0.033
2 (all)	0.09	0.35	0.06	0.49	0.009	0.053	0.003	0.028
3 (all)	0.09	0.35	0.07	0.49	0.003	0.080	0.003	0.032
4 (all)	0.09	0.36	0.09	0.46	0.005	0.076	0.006	0.026
L950 (all)	0.18	0.33	0.19	0.31	0.004	0.056	0.006	0.025
L2000 (all)	0.19	0.33	0.21	0.28	0.004	0.059	0.008	0.022
1 (attached)	0.04	0.19	0.01	0.38	0.002	0.056	0.000	0.017
2 (attached)	0.02	0.21	0.01	0.31	0.007	0.030	0.000	0.019
3 (attached)	0.02	0.20	0.01	0.30	0.000	0.060	0.000	0.021
4 (attached)	0.02	0.20	0.02	0.28	0.003	0.052	0.002	0.015
L950 (attached)	0.02	0.15	0.006	0.13	0.000	0.047	0.000	0.015
L2000 (attached)	0.02	0.14	0.007	0.11	0.000	0.053	0.000	0.014

TABLE 1. The numerical fraction of the number of objects identified in each region with respect to the total number of objects in that region, N_k , and the volume fraction that the objects occupy with respect to the volume of the mean boundary layer, V_k , at that region for all four different quadrant events indicated by the value of the subscript k from 1 to 4. L950 and L2000 correspond to the $Re_\tau = 950$ and $Re_\tau = 2000$ channel flow cases examined by Lozano-Durán *et al.* (2012).

3.1. Aspect ratios of attached eddies

Each identified cluster was circumscribed in boxes tightly bound to their streamwise, wall-normal, and spanwise extent. The probability density functions (PDFs) of the logarithms of the sizes of these bounding boxes are examined in Figures 2 and 3 across the different regions post breakdown to determine their scaling laws and how they compare to their counterparts in fully developed turbulent channel flow. For each of the objects identified, the sizes of the boxes are reported after being normalized by the local viscous length scale, $\delta_\nu = \nu/u_\tau$, at the location of the object’s centroid.

The streamwise and wall-normal size joint PDFs shown in Figure 2 illustrate that the two sizes follow the scaling law $\Delta_x = 3\Delta_y$ within all post-breakdown regions for both ejections and sweeps. This scaling law is the same one found by Lozano-Durán *et al.* (2012) for fully developed turbulent channel flow, indicating that the strong, attached, momentum-carrying structures develop asymptotic scaling laws almost immediately. The spanwise and wall-normal size joint PDFs shown in Figure 3 tell a similar story, with the geometrical scaling law $\Delta_z = \Delta_y$, observed in fully developed turbulent channel flow, emerging immediately after the breakdown point of the coherent Λ -vortices. While not shown here for brevity, the joint PDFs of the ratios between the streamwise-to-wall-normal and spanwise-to-wall-normal aspect ratios do not follow a linear scaling law but instead a quadratic one, $\Delta_x\Delta_y = 3\Delta_z^2$, illustrating the relative dispersion between the sizes of the objects in the streamwise and spanwise direction as they get taller. This is the same behavior observed in channel flows by Lozano-Durán *et al.* (2012).

3.2. Volumetric scaling and the fractal dimensions of attached eddies

The joint PDFs of the volume occupied by the ejections and sweeps (not the volume of their circumscribing box) versus their wall-normal extent are shown in Figure 4. The scaling law $V_{Q_k} = (2.5\Delta_y)^{2.25}$ is recovered by all the attached objects at all post-breakdown regions. This scaling law is consistent with the one found in fully developed turbulent channel flow.

If the objects are self-similar, the power law dependence of the volume on the object’s height can be used to infer the fractal dimension of these eddies. However, to avoid making that assumption, the fractal dimension of the attached eddies is computed directly using

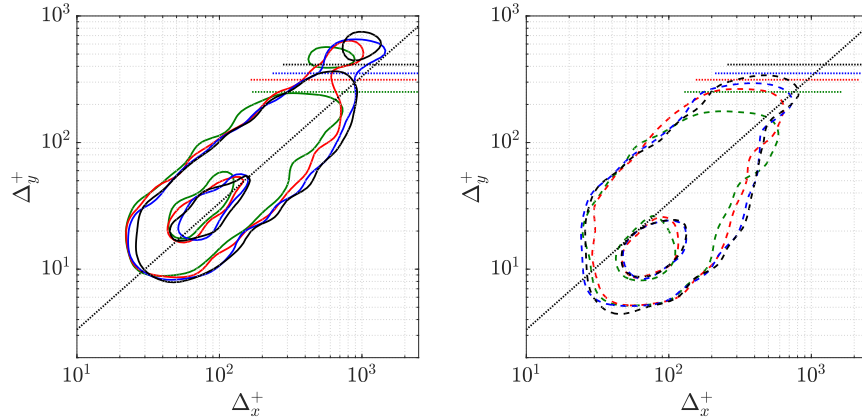


FIGURE 2. Joint PDFs of the logarithms of the sizes of the boxes circumscribing attached ejections and sweeps along the streamwise and wall-normal directions. The left plot with solid lines corresponds to ejections, and the right plot with dashed lines corresponds to the sweeps. The contours contain 25% and 95% of the total probability. The color coding is consistent with the regions defined in Figure 1, and the horizontal dashed lines represent the mean boundary layer thickness within that region. The diagonal black dashed lines correspond to the scaling law $\Delta_x = 3\Delta_y$.

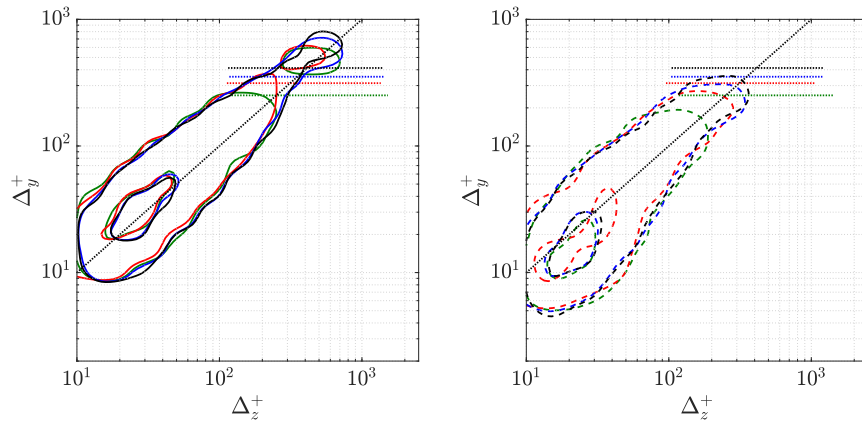


FIGURE 3. Joint PDFs of the logarithms of the sizes of the boxes circumscribing attached ejections and sweeps along the spanwise and wall-normal directions. Refer to the caption of Figure 2 for a description of all the lines, except the diagonal black dashed lines, which correspond to the scaling law $\Delta_z = \Delta_y$.

the box-counting technique as was done by Moisy & Jiménez (2004) and Lozano-Durán *et al.* (2012). The joint PDFs plotted in Figure 5 show that both the mean and the spread of the fractal dimension of the attached eddies collapse across the different regions. Away from the buffer layer, the sweeps and ejection PDFs collapse with respect to each other and are consistent with the contours found in fully developed channel flow, illustrating their similarity in the logarithmic region of the flow. Near the wall, the elongated tail of the sweeps reaching fractal dimensions close to one indicates the presence of more

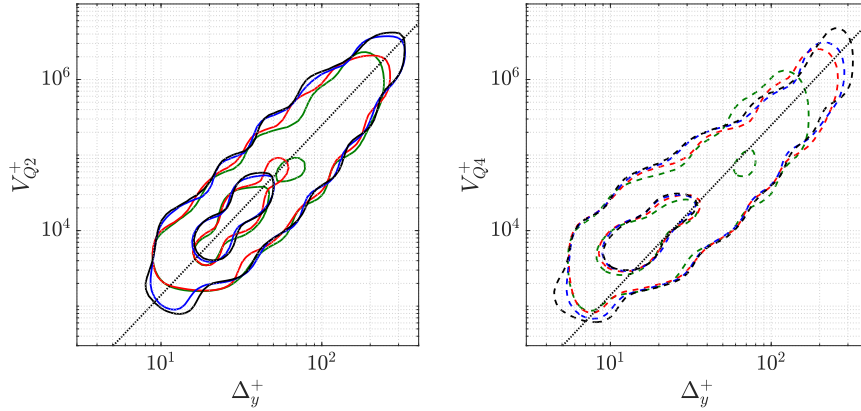


FIGURE 4. Joint PDFs of the volume occupied by ejections and sweeps compared to their wall-normal height normalized by the local viscous length scale, δ_ν . The diagonal dashed line corresponds to the scaling law $V_{Q_k} = (2.5\Delta_y)^{2.25}$. The contours contain 30% and 95% of the total probability. Refer to the caption of Figure 2 for a description of all the contours.

line-like structures, consistent once again with their counterparts from fully developed turbulent channel flow. By accounting for the increase in the thickness of the structures as they get taller, the mean fractal dimension is consistent with the volumetric scaling law.

The collapse of the fractal dimension joint PDFs illustrates that the high Reynolds number fractal signal is found as far upstream as the initial stages of transitional breakdown, which is consistent with the observations of Wu *et al.* (2020) where the fractal dimensions of the volume occupied by and the surface areas of turbulent/non-turbulent interfaces of spots followed the same scaling laws as the turbulent/non-turbulent interface of a fully developed turbulent boundary layer.

4. Conditional flow fields

While the geometrical scalings of the attached sweeps and ejections indicate that the asymptotic turbulent behavior is recovered immediately in the early stages of transitional breakdown, they do not quantify whether the flow field within and surrounding those transitional structures is more or less disordered than their counterparts in the fully developed turbulent region. The flow fields within and surrounding each identified structure in each region are extracted, rescaled, recentered, and averaged to provide the conditional flow field. The coordinates z^* and y^* are defined as

$$x_i^* \equiv \frac{x_i - x_i^o}{\Delta_y^o}, \tag{4.1}$$

where x_i^o and Δ_y^o are the location of the object’s centroid along each cardinal direction, i , and its height, respectively. During the conditional averaging procedure, the spanwise coordinate is realigned toward the nearest object of similar size and opposite sign of wall-normal velocity to prevent artificial symmetrization of the flow field. Only the structures that are attached are considered in this analysis.

Figure 6 illustrates the result of this procedure when the flow fields are centered around

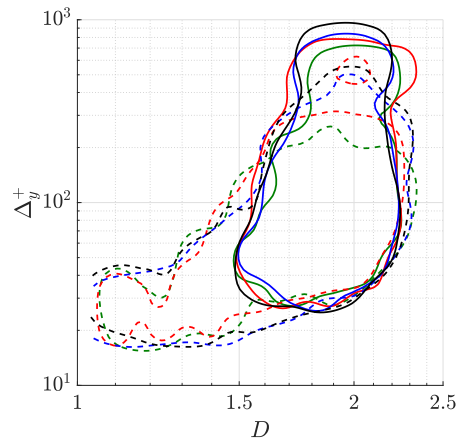


FIGURE 5. Joint PDF of the fractal dimension, D , versus the height of the attached ejections and sweeps normalized by the local viscous length scale, δ_ν^+ . Solid lines correspond to ejections, and dashed lines correspond to sweeps. The color coding is consistent with the partitioned regions in Figure 1. The contours contain 95% of the total probability.

ejections. A cross-section is shown at the streamwise center of the identified objects, i.e., $x^* = 0$. The flow field surrounding the ejections in the farthest downstream region matches those surrounding ejections when extracted from fully developed turbulent channel flow, as expected. The ejection coincides with a low-velocity streak flanked to one side by a high-velocity streak and a sweep. As we traverse the domain back upstream, the strength of both the positive and negative streaks increases. Furthermore, while the procedure avoids artificial symmetrization, a second positive streak emerges on the other side of the ejection within the first two regions of the flow. This coincides with an increase in the strength of the counter-rotating streamwise vortex to the left of the ejection.

The conditional flow fields indicate that the streamwise-aligned positive and negative streaks associated with the streamwise vortices exist in a regular spatial pattern upstream, and then get more disordered in their spatial positioning leading to a preference for the existence of one-sided pairs. However, it is also possible that the initial ordered pattern is due to a biased sampling of objects closer to the wall in regions one and two, which disappears when a larger separation of scale emerges downstream and the number of log-layer structures increases. Attempts at quantifying the disorder level by examining the flow field's conditional variance showed little differences across the different regions downstream of the transition. Similar observations are drawn from centering the conditional flow field around the sweep events.

5. Conclusions

Motivated by prior observations that conditional turbulent statistics far upstream in transitional turbulent boundary layers resemble those of fully developed turbulence, this study aimed at extending that comparison beyond single-point statistics to the geometrical properties of the dominant momentum-carrying structures. To do so, the clustering algorithm of Lozano-Durán *et al.* (2012) was adapted to extract the connected regions in space belonging to different momentum quadrants. Comparing the number and volume fractions of those extracted clusters to those found in a fully developed turbulent chan-

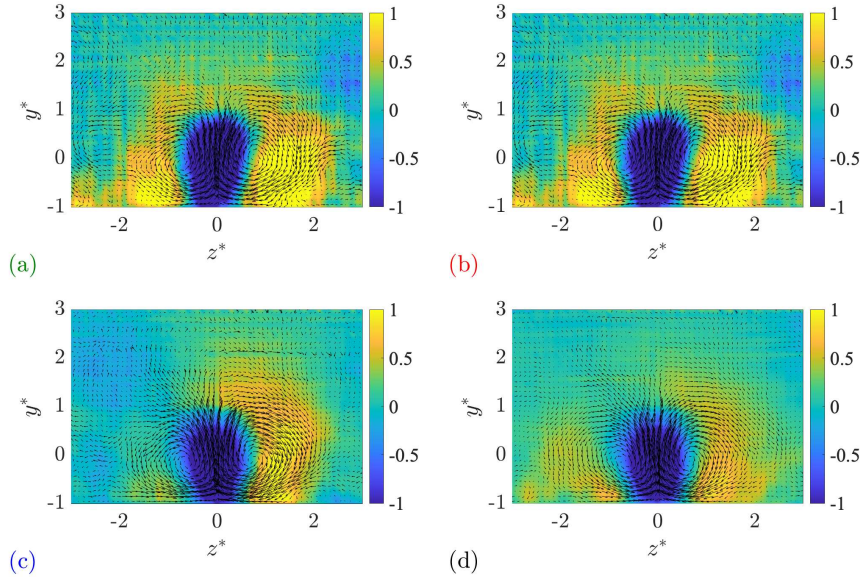


FIGURE 6. A cross-sectional flow field at $x^* = 0$ centered around ejection events. The colormap indicates the streamwise velocity, with darker colors corresponding to low velocity streaks and lighter colors corresponding to high velocity streaks. The arrows indicate the wall-normal and streamwise conditional cross flow. (a) Region 1. (b) Region 2. (c) Region 3. (d) Region 4.

nel flow indicated their high Reynolds number relative distribution is recovered almost immediately after the breakdown of the coherent Λ -vortices within less than one-third of an eddy-turnover length.

Given the attached eddies' dominant volume contribution in all four downstream regions, joint PDFs of their geometrical properties, namely their aspect ratios, streamwise-to-spanwise dispersion, occupied volume, and fractal dimensions, were computed. Across the four regions, the joint PDFs collapsed sufficiently to indicate that the asymptotic scaling laws hold immediately post breakdown. The attached ejections and sweeps obey the scaling laws $\Delta_x = 3\Delta_y$, $\Delta_z = \Delta_y$, $\Delta_x\Delta_y = 3\Delta_z^2$, and $V_{Q_k} = (2.5\Delta_y)^{2.25}$, as well as a mean fractal dimension $D \approx 2$ in the log-layer. These scaling laws are the same laws that apply to fully developed turbulent channel flows as observed by Lozano-Durán *et al.* (2012).

The conditional flow fields around ejection events were then examined for signs of order in the flow. It was found that the conditional flow fields got stronger in magnitude and displayed increasing symmetry the further upstream they were extracted. This is a signature of the stronger upstream spatial organization of the ejections and sweeps and the vortices that drive them. In essence, while the geometrical statistics of individual ejections and sweeps obey the fully turbulent scaling laws immediately post breakdown, their spatial organization in space changes further downstream, going from rows of ejections and sweeps to spatially disordered single pairs.

In conclusion, we have identified that the similarity between early transitional boundary layers and fully developed turbulent wall-bounded flows extends beyond standard statistics, such as the mean velocity profile and turbulent intensities, to all basic geometrical properties of the underlying momentum-carrying eddies. It is remarkable how

far upstream, after the breakdown of discrete Λ -vortices, the geometrical scalings hold, as they take less than one-third of an eddy-turnover length to emerge. To complete the comparison between transitional-turbulent and fully developed turbulent momentum-carrying structures, the analysis needs to be extended to their dynamical properties by utilizing the algorithms of Lozano-Durán & Jiménez (2014). This is in line with the future direction of research into turbulent spots dynamics, as highlighted by Wu (2022).

REFERENCES

- CANTWELL, B., COLES, D. & DIMOTAKIS, P. 1978 Structure and entrainment in the plane of symmetry of a turbulent spot. *J. Fluid Mech.* **87**, 641–672.
- CORINO, E. R. & BRODKEY, R. S. 1969 A visual investigation of the wall region in turbulent flow. *J. Fluid Mech.* **37**, 1–30.
- ELNAHNAS, A. & JOHNSON, P. L. 2022 On the enhancement of boundary layer skin friction by turbulence: an angular momentum approach. *J. Fluid Mech.* **940**, A36.
- ELNAHNAS, A., JOHNSON, P. L., LOZANO-DURÁN, A. & MOIN, P. 2019 On the evolution of the velocity gradient tensor in transitional boundary layers. *Annual Research Briefs*, Center for Turbulence Research, Stanford University, pp. 211–222.
- EMMONS, H. W. 1951 The laminar-turbulent transition in a boundary layer—Part I. *J. Aeronaut. Sci.* **18**, 490–498.
- HENNINGSON, D., SPALART, P. & KIM, J. 1987 Numerical simulations of turbulent spots in plane poiseuille and boundary-layer flow. *Phys. Fluids* **30**, 2914–2917.
- KLINE, S. J., REYNOLDS, W. C., SCHRAUB, F. & RUNSTADLER, P. 1967 The structure of turbulent boundary layers. *J. Fluid Mech.* **30**, 741–773.
- LOZANO-DURÁN, A., FLORES, O. & JIMÉNEZ, J. 2012 The three-dimensional structure of momentum transfer in turbulent channels. *J. Fluid Mech.* **694**, 100–130.
- LOZANO-DURÁN, A., HACK, M. & MOIN, P. 2018 Modeling boundary-layer transition in direct and large-eddy simulations using parabolized stability equations. *Phys. Rev. Fluids* **3**, 023901.
- LOZANO-DURÁN, A. & JIMÉNEZ, J. 2014 Time-resolved evolution of coherent structures in turbulent channels: characterization of eddies and cascades. *J. Fluid Mech.* **759**, 432–471.
- MARXEN, O. & ZAKI, T. A. 2019 Turbulence in intermittent transitional boundary layers and in turbulence spots. *J. Fluid Mech.* **860**, 350–383.
- MOISY, F. & JIMÉNEZ, J. 2004 Geometry and clustering of intense structures in isotropic turbulence. *J. Fluid Mech.* **513**, 111–133.
- PARK, G. I., WALLACE, J. M., WU, X. & MOIN, P. 2012 Boundary layer turbulence in transitional and developed states. *Phys. Fluids* **24**, 035105.
- SAYADI, T., HAMMAN, C. W. & MOIN, P. 2013 Direct numerical simulation of complete H-type and K-type transitions with implications for the dynamics of turbulent boundary layers. *J. Fluid Mech.* **724**, 480–509.
- SILLERO, J. A., JIMÉNEZ, J. & MOSER, R. D. 2013 One-point statistics for turbulent wall-bounded flows at Reynolds numbers up to $\delta^+ \approx 2000$. *Phys. Fluids* **25**, 105102.
- WALLACE, J. M., ECKELMANN, H. & BRODKEY, R. S. 1972 The wall region in turbulent shear flow. *J. Fluid Mech.* **54**, 39–48.
- WU, X. 2022 New insights into turbulent spots. *Annu. Rev. Fluid Mech.* **55**, 45–75.
- WU, X., MOIN, P., WALLACE, J. M., SKARDA, J., LOZANO-DURÁN, A. & HICKEY,

- J.-P. 2017 Transitional-turbulent spots and turbulent-turbulent spots in boundary layers. *Proc. Natl. Acad. Sci.* **114**, E5292–E5299.
- WU, Z., ZAKI, T. A. & MENEVEAU, C. 2020 High-Reynolds-number fractal signature of nascent turbulence during transition. *Proc. Natl. Acad. Sci.* **117**, 3461–3468.